

values of the charge densities σ_- and $\sigma_{+,av}$, although we must have $|\sigma_-| > \sigma_{+,av}/2$ in order to obtain the instability. Increasing the salt concentration beyond $\hat{n} = 20$ mM, however, eliminates charge reversal by increasing τ , a prediction in qualitative agreement with the experiments of (3). If \hat{n} lies between 20 mM and ~ 150 mM, we still find an instability, this time to partitioning into strong- and weak-adhesion zones (2).

In retrospect, our mechanism is reminiscent of the chemiosmotic principle in bioenergetics (14): In this context it is well known that electrostatic effects can be transmitted over many screening lengths with the help of a semipermeable membrane. Besides entering into an explanation of the experiments in (2, 3), our mechanism predicts that flaccid charged vesicles can adhere to oppositely charged substrates while remaining flaccid. Our analysis also makes testable predictions about the dependence of the equilibrium area fraction γ_* on the system parameters, notably the bilayer composition and salt concentration. Perhaps most strikingly, the charge-reversed zone we describe should prove attractive to same-charge objects—a phenomenon not yet seen.

References and Notes

- S. A. Safran, *Statistical Thermodynamics of Surfaces, Interfaces, and Membranes* (Addison-Wesley, Reading, MA, 1994).
- J. Nardi, R. Bruinsma, E. Sackmann, *Phys. Rev. E* **58**, 6340 (1998).
- L. Ramos, T. C. Lubensky, N. Dan, P. Nelson, D. A. Weitz, unpublished results.
- Changes in the materials used had little effect on the experimental results in (3). We used colloidal spheres of diameters 0.98, 0.83, and 1.00 μm , with sulfate groups, sulfate and carboxylate groups, and carboxylate and amine groups, respectively. Electrophoretic velocity measurements confirmed that all types of particles were negatively charged in our experimental conditions. All three samples behaved similarly in the experiments. We also varied the bilayer characteristics through the addition of octanol. Although this co-surfactant is known to alter the curvature-elasticity properties of bilayers, we could not see any qualitative effect on our results at alcohol-to-Triton-X weight ratios ranging from 0 to 0.7. In Fig. 1, the weight ratio DDAB (didodecyl dimethyl ammonium bromide):Triton:octanol was 1:0.37:0.13. The buffer solution contained NaCl at concentrations from 1 to 10 mM, as discussed below.
- R. B. Gennis, *Biomembranes* (Springer-Verlag, New York, 1989).
- W. M. Gelbart and R. Bruinsma, *Phys. Rev. E* **55**, 831 (1997).
- Y. Chen and P. Nelson, unpublished results.
- V. A. Parsegian and D. Gingell, *Biophys. J.* **12**, 1192 (1972).
- We work in SI units. Thus, $\epsilon_0 = 9 \times 10^{-12}$ F/m, the potential around a point charge q in vacuum is $\psi(r) = q/4\pi\epsilon_0 r$, and so forth.
- We need not assume the membrane to be impermeable to water; because the bulk salt concentration is assumed the same on both sides, there will be no net osmotic flow.
- A third exchanged quantity, the net counterion charge density outside the membrane, is then fixed by charge neutrality: $\sigma_0 = -(\sigma_+ + \sigma_-)$. Similarly, the density of neutral surfactants in the membrane is not independent, being given by $(2/a_0) - (\sigma_+/e)$. The numbers of individual counterions of each species are not, however, conserved, because neutral $+/-$ pairs can be exchanged with large reservoirs (the bulk solution inside and outside the vesicle) without macroscopic charge separation.
- Poisson-Boltzmann theory is a mean-field approximation. It is well known that correlated fluctuations can cause surprising effects if the counterions are multivalent. For example, like-charged parallel plates can have attractive regimes (15, 16), although we are not aware of a similar prediction of repulsion for opposite charges. Correlation effects are generally small if the ions are univalent, as in the experiment of (3). The physical mechanism we present, in contrast, arises already in mean-field theory; it does not rely on any fluctuation effects (nor on finite ion-size effects). Including such effects does not materially change our conclusions (7). Other colloidal forces not included in our analysis (for example solvation forces) are short-ranged; our effect relies on the physics of surfaces when they are separated by more than a nanometer.
- The extent of coverage is not directly measurable, since the degree to which each colloidal sphere is engulfed by membrane is not observed. In addition, the actual situation in Fig. 1 may not be in equilibrium. Our point is simply that our theory explains why the vesicle in Fig. 1 has stopped attracting further colloidal particles.
- R. J. Nossal and H. Lecar, *Molecular and Cell Biophysics* (Addison-Wesley, Redwood City, CA, 1991).
- L. Guldbrand, B. Jönsson, H. Wennerström, P. Linse, *J. Chem. Phys.* **80**, 2221 (1984).
- I. Rouzina and V. A. Bloomfield, *J. Phys. Chem.* **100**, 9977 (1996).
- We thank R. Bruinsma and S. Safran for discussions; J. Crocker, K. Krishana, and E. Weeks for experimental assistance; and J. Nardi for communicating results to us before publication. N.D. was supported in part by NSF grant CTS-9814398; T.C.L., L.R., and D.A.W. were supported in part by NSF Materials Research and Engineering Center Program under award number DMR96-32598 and equipment grants DMR97-04300 and DMR97-24486; P.N. was supported in part by NSF grant DMR98-07156; L.R. was supported in part by a Bourse Lavoisier from the Ministère des Affaires Étrangères de France.

12 March 1999; accepted 15 June 1999

Climate and Satellite Indicators to Forecast Rift Valley Fever Epidemics in Kenya

Kenneth J. Linthicum,^{1*} Assaf Anyamba,^{2*} Compton J. Tucker,² Patrick W. Kelley,¹ Monica F. Myers,² Clarence J. Peters³

All known Rift Valley fever virus outbreaks in East Africa from 1950 to May 1998, and probably earlier, followed periods of abnormally high rainfall. Analysis of this record and Pacific and Indian Ocean sea surface temperature anomalies, coupled with satellite normalized difference vegetation index data, shows that prediction of Rift Valley fever outbreaks may be made up to 5 months in advance of outbreaks in East Africa. Concurrent near-real-time monitoring with satellite normalized difference vegetation data may identify actual affected areas.

Rift Valley fever (RVF), a viral disease first described in Kenya in 1931 (1), affects domestic animals and humans throughout sub-Saharan Africa and results in widespread livestock losses and frequent human mortality. Its occurrence is known to follow periods of widespread and heavy rainfall associated with the development of a strong intertropical convergence zone, the region in the equatorial tropics where air currents from the north and south converge and produce precipitation (2). Such heavy rainfall floods mosquito breeding habitats in East Africa, known as "dambos," which contain transovarially infected *Aedes* mosquito eggs and subsequently serve as good habitats for other *Culex* species mosquito vectors (3). The most recent RVF

epizootic/epidemic was in East Africa in late 1997 and early 1998.

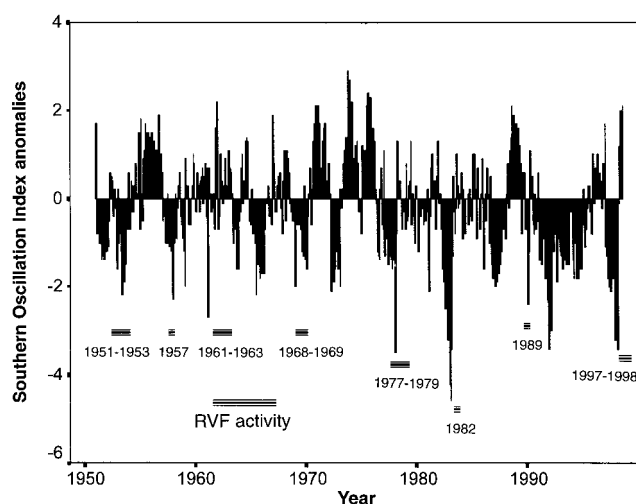
Vegetation responds to increased rainfall and can be easily measured by satellite. Normalized difference vegetation index (NDVI) data from the advanced very high resolution radiometer (AVHRR) on National Oceanic and Atmospheric Administration (NOAA) satellites have been used to detect conditions suitable for the earliest stages in an RVF epizootic (4). Refinement in determining the spatial distribution of RVF viral activity, through identification of ideal mosquito habitat, has been possible with higher resolution Landsat, Systeme pour l'Observation de la Terre (SPOT), and airborne synthetic aperture radar data (5); however, predictive indicators are needed to forecast RVF outbreaks. Here we show that several climate indices can be used to predict outbreaks up to 5 months in advance.

The El Niño–Southern Oscillation (ENSO) phenomenon is a principal cause of global interannual climate variability (6, 7). Warm ENSO events are known to increase precipi-

¹Department of Defense, Global Emerging Infections System, Division of Preventive Medicine, Walter Reed Army Institute of Research, Washington, DC 20307-5100, USA. ²Earth Sciences Directorate, NASA Goddard Space Flight Center, Greenbelt, MD 20771, USA. ³Special Pathogens Branch, Centers for Disease Control and Prevention, Atlanta, GA 30333, USA.

*To whom correspondence should be addressed.

Fig. 1. A time series plot of SOI anomalies between January 1950 and May 1998. Periods of RVF activity in Kenya are depicted. Monthly SOI values are shown as standardized deviations based on the 1951–80 mean.



tation in some regions of East Africa and result in droughts in southern Africa (7, 8). The Southern Oscillation Index (SOI) is the most commonly used index for the ENSO phenomena (7, 9) and extends back to the late 19th century. This index compares atmospheric pressure in Tahiti with that of Darwin, Australia, and is expressed as a standardized deviation from the norm. Strong negative anomalies are associated with an El Niño event (6, 10). Anomalous climatic conditions caused by ENSO are now recognized to be linked with outbreaks of various human and livestock diseases in various countries (7). Above normal East African rainfall is associated with negative SOI anomalies resulting in more green vegetation, which then is detected by the satellite-derived NDVI (11, 12).

We compared RVF virus activity with corresponding monthly SOI from 1950 to 1998, sea surface temperatures (SSTs) from an equatorial region in the Pacific Ocean (named NINO 3.4, 5°N to 5°S, 170° to 120°W), equatorial western Indian Ocean SSTs (10°N to 10°S, 40° to 64°E), and Kenyan NDVI AVHRR data from 1982 to 1998 (13). During this 48-year period, there were eight periods with RVF viral activity and 13 periods when there were strong negative anomalies in the SOI (< -1.5) (Fig. 1).

Rainfall exceptionally above normal was coincident with major regional RVF epizootics in 1951–53, 1961–63, 1968–69, 1977–79, and 1997–98 (2). In late 1957 and 1982 and in the middle of 1989, heavy rainfall in Kenya preceded RVF virus activity that was detected by identification of clinical cases, isolation of the virus in mosquitoes, or detection of high levels of immunoglobulin (type IgM) antibody specific for RVF virus (indicating recent RVF infection) in domestic animals and humans (2, 3, 14).

RVF activity and above normal rainfall always followed a period of strong negative

deviation of the SOI; however, neither the strength nor the length of the SOI anomaly correlated with the intensity of RVF activity. The regional RVF activity detected in 1982 followed an intense SOI anomaly < -4 , whereas the major outbreaks starting in 1951, 1961, and 1968 occurred after SOI anomalies < -2 . Strong negative SOI anomalies also occurred in 1964, 1969, 1972–73, 1981, and 1991–95; however, there was neither above normal rainfall nor detectable RVF activity in Kenya for these periods. Although excessively heavy rainfall and RVF activity in Kenya were dependent on a strong SOI anomaly, the overall ability to predict an RVF outbreak with SOI anomalies alone was only 67%, indicating that other factors must be involved.

A strong relation between equatorial Pacific SST and elevated East African precipitation has been reported (8, 12), as has a strong relation between equatorial Pacific SST and maize yield in Zimbabwe (15). In addition, Indian Ocean SST has been reported to be highly related to rainfall in East Africa (16).

Concurrent Pacific and Indian Ocean SST anomalies $> 3^{\circ}\text{C}$ and 0.5°C , respectively, were correlated with widespread rains in East Africa (8, 12, 16) and RVF outbreaks. RVF activity was followed by 2 (1982–83) and 5 (1997–98) months of strong concurrent equatorial Pacific and Indian Ocean SST anomalies (Fig. 2). When both equatorial Pacific and Indian Ocean SSTs were elevated, the extent of the Indian Ocean temperature anomaly was indicative of the intensity and the duration of RVF activity. However, when the strength of the concurrent Pacific and Indian Ocean SST anomalies was reduced, but still positive, the pattern of increased rainfall can be irregular and a region-wide effect cannot usually be found.

To overcome the problem of determining

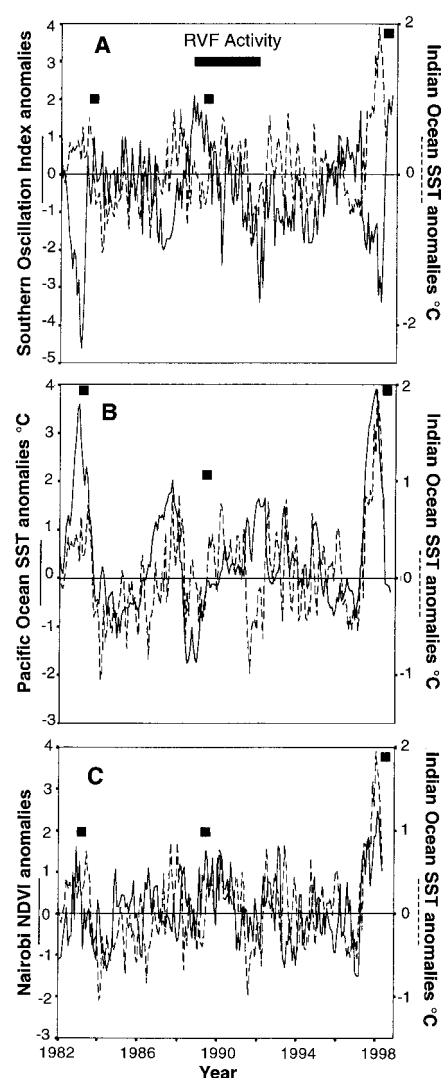
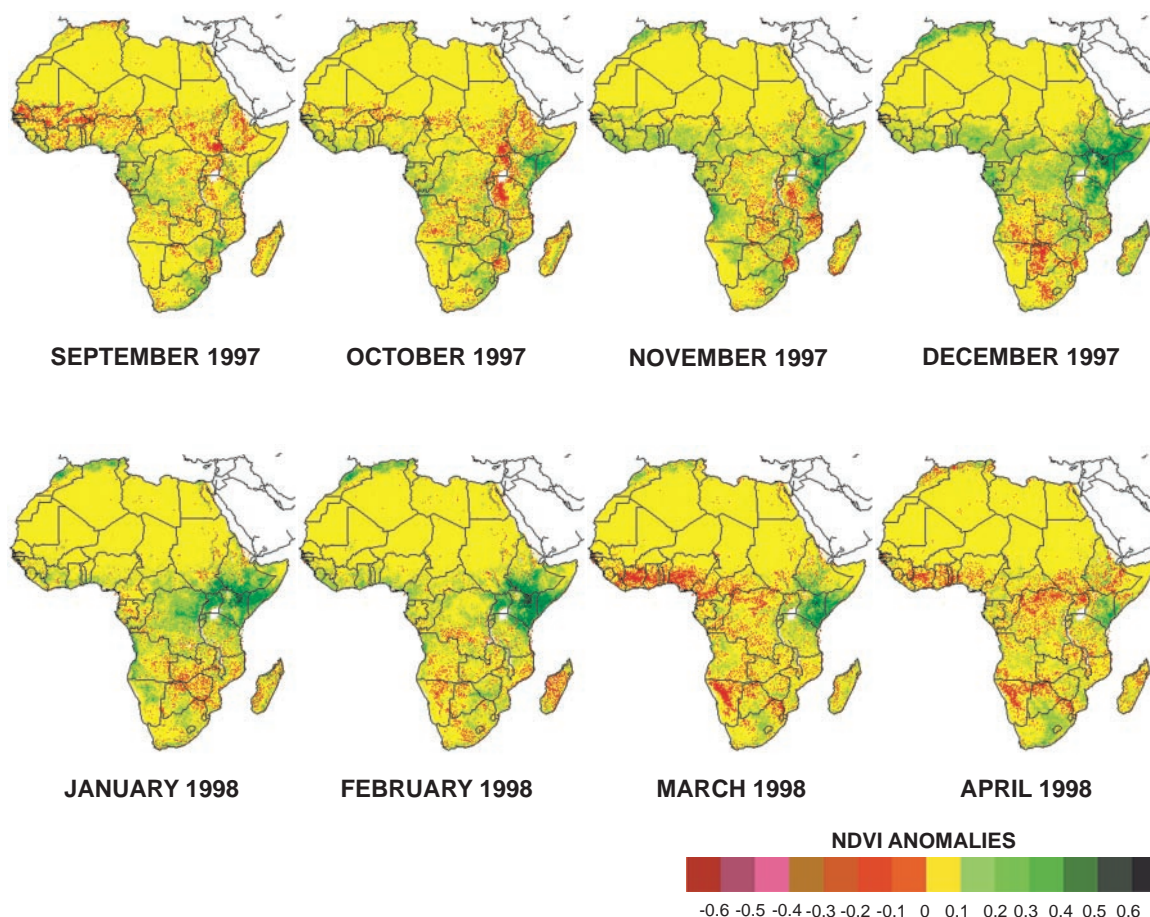


Fig. 2. Time series plots of Indian Ocean SST anomalies from January 1982 to May 1998 with SOI anomalies (A), equatorial Pacific Ocean (Niño 3.4 area) SST anomalies (B), and Nairobi NDVI anomalies (C). Indian and equatorial Pacific Ocean SST anomalies are depicted as degree Celsius deviations from their respective mean value (mean value for period shown = 0°C). SOI and Nairobi NDVI anomalies are depicted as deviations from their respective mean values normalized by the standard deviation (mean value for period shown = 0).

where, and to what extent, RVF outbreaks were possible in years lacking concurrently high Pacific and Indian Ocean SST anomalies, we used NDVI measurements derived from NOAA polar-orbiting satellite data to identify areas of abnormally high green vegetation development resulting from abnormally high rainfall (17). This is possible through the use of intercalibrated satellite data running from 1981 through the present (18).

We suggest that NOAA AVHRR NDVI time series data are required to identify more localized areas where anomalous rainfall has

Fig. 3. Monthly AVHRR NDVI composite images of continental Africa during the 1997–98 ENSO warm event. Data depicted are the degree of deviation from the long-term mean calculated for the period January 1982 to May 1998 in NDVI units (13). A value of zero means that current values are identical to the monthly 1982–95 mean.



occurred and hence more localized RVF activity is present. It is only by doing this discrimination that lower amounts of RVF can be confirmed or, conversely, that a lower threshold of rainfall anomalies coupled with extent of affected area can be determined as this relates to RVF activity outbreaks. The satellite normalized difference vegetation data are available the same day as acquisition, provide confirmation of predicted rainfall events with SSTs, and provide direct identification of localized rainfall anomalies.

Elevated NDVI anomalies, as indicated by dark green shades in Fig. 3, were observed for East Africa starting in October 1997 (the start of the normal short rainy period) and extending to April 1998 (through the normal dry season of January and February) (Fig. 3). NDVI anomalies were significantly correlated with RVF activity 1 to 2 months before detection of viral activity ($P < 0.5$) (19).

Strong NDVI positive anomalies were observed in June 1989 with the presence of RVF activity and in January and February 1993 in the absence of detectable RVF activity (Fig. 2C). We suggest that the elevated NDVI values at these times reflected local rain conditions because they were not observed in NDVI anomaly data for the same

period at other locations in Kenya.

To determine the best predictors of RVF activity, we evaluated SOI, equatorial Pacific SSTs, Indian Ocean SSTs, and NDVI anomalies in various combinations in ARIMA models (20). The best fit to the RVF outbreak data was achieved when equatorial Pacific and Indian Ocean SST and NDVI anomaly data were used together (ARIMA, SBC = -106, analysis of variance $df = 192$, $P < 0.01$). These data could have been used to successfully predict each of the three RVF outbreaks that occurred between 1982 and 1998 without predicting any false RVF events for an overall prediction of risk of 100%. Predictive models that use either SOI and Indian Ocean or NDVI and Indian Ocean anomaly data would have predicted all three RVF events but falsely predicted either one or two disease events, respectively.

The ability to forecast regional RVF virus activity in Kenya, based on Pacific and Indian Ocean SST anomalies and NDVI, 2 to 5 months before outbreaks could permit vaccination of domestic animals and pretreatment of mosquito habitats adjacent to domestic animal herds and human habitations with highly effective sustained release insecticides that would be released upon flooding (21).

References and Notes

1. R. Daubney, J. R. Hudson, P. C. Garnham, *J. Pathol. Bacteriol.* **34**, 545 (1931).
2. F. G. Davies, K. J. Linthicum, A. D. James, *Bull. W.H.O.* **63**, 941 (1985).
3. K. J. Linthicum, F. G. Davies, A. Kairo, C. L. Bailey, *J. Hyg.* **95**, 197 (1985).
4. K. J. Linthicum, C. L. Bailey, F. G. Davies, C. J. Tucker, *Science* **235**, 1656 (1987).
5. K. O. Pope et al., *Remote Sens. Environ.* **40**, 185 (1992); K. J. Linthicum et al., *Sist. Terra* **3**, 44 (1994).
6. M. A. Cane, *Annu. Rev. Earth Planet. Sci.* **14**, 43 (1986).
7. M. H. Glantz, in *Teleconnections Linking World Wide Climate Anomalies: Scientific Basis and Societal Impact*, M. H. Glantz, R. W. Katz, N. Nicholls Eds. (Cambridge Univ. Press, New York, 1991), pp. 1–12; N. Nicholls, in *Teleconnections Linking World Wide Climate Anomalies: Scientific Basis and Societal Impact*, M. H. Glantz, R. W. Katz, N. Nicholls Eds. (Cambridge Univ. Press, New York, 1991), pp. 493–510.
8. C. Ropelewski and M. Halpert, *Mon. Weather Rev.* **115**, 2352 (1987).
9. C. Chagas and G. Puppi, in *Persistent Meteorological-Oceanographic Anomalies and Teleconnections*, C. Chagas and G. Puppi, Eds. (Pontificia Academia Scientiarum, Citta Del Vaticano, 1986), pp. 1–15.
10. E. M. Rasmusson, in *Teleconnections Linking World Wide Climate Anomalies: Scientific Basis and Societal Impact*, M. H. Glantz, R. W. Katz, N. Nicholls, Eds. (Cambridge Univ. Press, New York, 1991), pp. 309–343.
11. A. Anyamba and J. R. Eastman, *Int. J. Remote Sens.* **17**, 2533 (1996); G. Farmer, *J. Climatol.* **8**, 489 (1988).
12. R. B. Myneni, S. O. Los, C. J. Tucker, *Geophys. Res. Lett.* **23**, 729 (1996).
13. NDVI data were processed after C. J. Tucker, W. W.

- Newcomb, and H. E. Dregne [*Int. J. Remote Sens.* **15**, 3547 (1994)]. SOI and SST data are produced and archived by the National Oceanographic and Atmospheric Administration/Climate Prediction Center (<http://www.cpc.ncep.noaa.gov/>). A previous paper (4) proposed the use of a satellite-derived potential virus activity factor. We now use monthly NDVI data, normalized to represent departures from the 1982–95 mean, to better characterize rainfall anomalies associated with RVF activity.
14. T. M. Logan, K. J. Linthicum, F. G. Davies, Y. S. Binopal, C. R. Roberts, *J. Med. Entomol.* **28**, 293 (1991); T. M. Logan, F. G. Davies, K. J. Linthicum, T. G. Ksiazek, *Trans. R. Soc. Trop. Med. Hyg.* **86**, 202 (1992).
 15. M. A. Cane, G. Eshel, R. W. Buckland, *Nature* **370**, 204 (1994).
 16. S. E. Nicholson, *Int. J. Climatol.* **17**, 345 (1997); _____ and J. Kim, *ibid.*, p. 117.
 17. There is a direct relation between rainfall and green vegetation growth, between green vegetation growth

- and the NDVI, and hence between rainfall and the NDVI. This relation applies to areas receiving precipitation of <800 mm/year. W. K. Lauenroth, in *Perspectives in Grassland Ecology*, N. French, Ed. (Springer-Verlag, New York, 1979), pp. 3–24; H. N. Le Houerou and C. H. Hoste, *J. Range Manage.* **30**, 181 (1977); A. R. Malo and S. E. Nicholson, *J. Arid Environ.* **19**, 1 (1990); S. E. Nicholson, M. L. Davenport, A. R. Malo, *Clim. Change* **17**, 209 (1990); C. J. Tucker and S. E. Nicholson, *Ambio*, in press.
18. B. N. Holben, Y. J. Kaufman, J. D. Kendall, *Int. J. Remote Sens.* **11**, 1511 (1990); E. F. Vermote and Y. J. Kaufman, *ibid.* **16**, 2317 (1995); S. O. Los, *ibid.* **14**, 1907 (1994); N. Che and J. C. Price, *Remote Sens. Environ.* **41**, 19 (1992).
 19. Correlation coefficients were determined for a data series calculated by the differences between adjacent values with SPSS Trends 6.1 software (SPSS, Chicago, 1994). Nairobi NDVI anomalies were derived from average monthly composite data within

- 8 by 8 grid cells, each with a spatial resolution of 8 km centered close to Nairobi, Kenya. Monthly AVHRR data were derived from global area coverage data that are produced by the on-board processing of large area coverage data (1.1 km by 1.1 km) and subsequently transmitted to receiving stations in Virginia or Alaska. Composite data were formed by selecting the highest NDVI for each grid cell location from daily data for that month to minimize cloud and atmospheric contamination. NDVI data were calculated and mapped to a Hammer-Aitof projection. The highest value during a monthly period was selected to represent the monthly composite for each grid cell location.
20. Autoregressive Integrated Moving Average (ARIMA) analysis determined by SPSS, Trends 6.1 software.
 21. T. M. Logan et al., *J. Am. Mosq. Control Assoc.* **6**, 736 (1990).

5 February 1999; accepted 5 May 1999

Unraveling the Electronic Structure of Individual Photosynthetic Pigment-Protein Complexes

Antoine M. van Oijen,^{1*} Martijn Ketelaars,² Jürgen Köhler,^{1†} Thijs J. Aartsma,² Jan Schmidt¹

Low-temperature single-molecule spectroscopic techniques were applied to a light-harvesting pigment-protein complex (LH2) from purple photosynthetic bacteria. The properties of the electronically excited states of the two circular assemblies (B800 and B850) of bacteriochlorophyll a (BChl a) pigment molecules in the individual complexes were revealed, without ensemble averaging. The results show that the excited states of the B800 ring of pigments are mainly localized on individual BChl a molecules. In contrast, the absorption of a photon by the B850 ring can be consistently described in terms of an excitation that is completely delocalized over the ring. This property may contribute to the high efficiency of energy transfer in these photosynthetic complexes.

The primary process in bacterial photosynthesis is the absorption of a photon by the light-harvesting antenna system, followed by the rapid and efficient transfer to the reaction center where the charge separation takes place. Typically, photosynthetic purple bacteria contain two types of antenna complexes, light-harvesting complexes 1 and 2 (LH1 and LH2, respectively), both of which are integral membrane proteins. The reaction center is presumed to be surrounded by the LH1 complex, whereas the LH2 complexes are arranged around the perimeter of the LH1 ring in a two-dimensional structure (1). The structure of the LH2 complex of the purple bacterium *Rhodospseudomonas acidophila* is known in great detail from x-ray

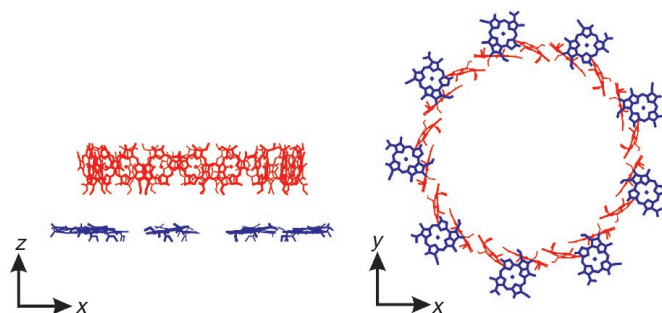
crystallography (2), which has shown that the LH2 complex comprises 27 BChl a and (presumably) 18 carotenoid molecules noncovalently bound to the protein matrix. The BChl a molecules are organized in two concentric rings (Fig. 1). One ring, referred to as B800, features a group of nine well-separated BChl a molecules with an absorption band at ~800 nm. The other ring, referred to as B850, consists of 18 closely interacting BChl a molecules with an absorption band at ~860 nm. The entire LH2 complex is cylindrically symmetric with a

ninefold symmetry axis. Upon excitation, energy transfer occurs from B800 to B850 molecules on a picosecond time scale (3–5), whereas among the B850 molecules, it is an order of magnitude faster (6–8). The transfer of energy from LH2 to LH1 and subsequently to the reaction center occurs in vivo on a time scale of 5 to 25 ps (9), very fast in comparison to the decay of B850 in isolated LH2, which corresponds to a lifetime of 1.1 ns.

Despite the fact that the LH2 complex has been intensively investigated in recent years with a wide variety of spectroscopic tools, including the observation of the fluorescence dynamics of single LH2 complexes (10), no clear picture of the electronic structure of its excited states exists. Here, we present the results of a study of isolated single LH2 complexes by single-molecule fluorescence-excitation spectroscopy, a method successfully applied in recent years to the detection of single guest molecules in crystalline and amorphous matrices (11). This technique allows the observation of optical spectra of individual complexes devoid of the ensemble averaging over static intercomplex disorder, thus directly revealing the salient properties of the electronic structure of the excited states.

The LH2 complexes of *R. acidophila* were prepared as described elsewhere (3). Hydrolyzed poly(vinyl alcohol) (PVA) with a weight-average molecular weight of 125,000 (obtained from British Drug House) was purified over a

Fig. 1. Geometrical arrangement of the 27 BChl a molecules of the LH2 complex of *R. acidophila* obtained by x-ray crystallography. The B800 BChl a molecules are depicted in blue, and the B850 pigments are red. The phytol chains of the BChl a molecules are omitted for clarity. The data have been taken from the Protein Data Bank (identification code: 1kzu).



¹Centre for the Study of Excited States of Molecules, ²Department of Biophysics, Huygens Laboratory, Leiden University, Post Office Box 9504, 2300 RA Leiden, Netherlands.

*To whom correspondence should be addressed. E-mail: antoine@molphys.leidenuniv.nl
[†]Present address: Ludwig-Maximilians-Universität München, Sektion Physik und Center for NanoScience, Lehrstuhl für Photonik und Optoelektronik, Amalienstrasse 54, 80799 München, Germany.

Climate and Satellite Indicators to Forecast Rift Valley Fever Epidemics in Kenya

Kenneth J. Linthicum, Assaf Anyamba, Compton J. Tucker, Patrick W. Kelley, Monica F. Myers and Clarence J. Peters

Science **285** (5426), 397-400.
DOI: 10.1126/science.285.5426.397

ARTICLE TOOLS

<http://science.sciencemag.org/content/285/5426/397>

REFERENCES

This article cites 21 articles, 1 of which you can access for free
<http://science.sciencemag.org/content/285/5426/397#BIBL>

PERMISSIONS

<http://www.sciencemag.org/help/reprints-and-permissions>

Use of this article is subject to the [Terms of Service](#)

Science (print ISSN 0036-8075; online ISSN 1095-9203) is published by the American Association for the Advancement of Science, 1200 New York Avenue NW, Washington, DC 20005. The title *Science* is a registered trademark of AAAS.

Copyright © 1999 The Authors, some rights reserved; exclusive licensee American Association for the Advancement of Science. No claim to original U.S. Government Works.